All-Dielectric Crescent Metasurface Sensor Driven by Bound States in the Continuum

Juan Wang, Julius Kühne, Theodosios Karamanos, Carsten Rockstuhl, Stefan A. Maier, and Andreas Tittl*

Metasurfaces based on quasi-bound states in the continuum (quasi-BICs) constitute an emerging toolkit in nanophotonic sensing as they sustain high quality factor resonances and substantial near-field enhancements. It is demonstrated that silicon metasurfaces composed of crescent shaped meta-atoms provide tailored light-matter interaction controlled by the crescent geometry. Significantly, this metasurface not only exhibits a fundamental quasi-BIC resonance, but also supports a higher-order resonance with tunable electromagnetic field enhancement and advantageous properties for sensing. The higher-order resonance shows twice the sensitivity of the fundamental one for bulk refractive index sensing. It is further demonstrated that both the fundamental and higher-order resonances can be exploited for sensing ultrathin layers of biomolecules in air and buffer solutions. Specifically, when measuring in buffer solution, the figure of merit of the sensor, defined as the change in the spectral position of the resonance normalized to its full width at half maximum, is a factor of 2.5 larger for the higher-order resonance when compared to the fundamental one. Due to its high sensitivity and potential for straightforward microfluidic integration, the silicon crescent metasurface is ideally suited for real-time and in situ biosensing, enabling compact sensing devices for a wide range of diagnostic applications.

1. Introduction

The development of biosensors with fast response, high accuracy, and capability for real-time and on-site detection has become increasingly significant for human well-being, especially for the diagnosis and treatment monitoring of infectious disease threats. Biosensors require high sensitivity, high

specificity, and should approach diagnostically relevant detection limits. In this challenging field, optical sensors based on photonic nanostructures stand out among other approaches thanks to their advantages of versatile surface functionalization for high specificity, label-free detection for multiplexed assays, and high sensitivity for molecular identification and monitoring kinetic binding processes.[1–3] Plasmonic nanostructures/nanomaterials, as prototypical examples for photonic nanostructures, act as transducers that have been well investigated for biological sensing owing to their enhanced near-field confinement at the surface driven by localized surface plasmon resonances, which are extremely sensitive to changes in the local environment.[4] However, plasmonic resonances are typically fairly broad (as quantified by the full width at half maximum, FWHM) due to the intrinsic losses of plasmonic materials, which strongly limits their sensitivity. Therefore, high refractive index dielectric nanomaterials/nanostructures[5,6] have seen surging interest for sensing as they sustain resonances with a much narrower FWHM and enhanced quality (Q) factors and near-field confinement. All-dielectric nanostructures have opened a new branch of nanophotonics thanks to their capability of manipulating both the electric and magnetic components of the incident light.[7] The improved Q factor and strongly enhanced

J. Wang, J. Kühne, S. A. Maier, A. Tittl
Chair in Hybrid Nanosystems
Nanoinstitute Munich
Faculty of Physics
Ludwig-Maximilians-Universität München
80539 München, Germany
E-mail: andreas.tittl@physik.uni-muenchen.de

T. Karamanos, C. Rockstuhl
Institute of Theoretical Solid State Physics
Karlsruhe Institute of Technology
76131 Karlsruhe, Germany
C. Rockstuhl
Institute of Nanotechnology
Karlsruhe Institute of Technology
76021 Karlsruhe, Germany
S. A. Maier
The Blackett Laboratory
Department of Physics
Imperial College London
London SW7 2AZ, UK

**ADVANCED
SCIENCE NEWS**

www.advancedsciencenews.com

**ADVANCED
FUNCTIONAL
MATERIALS**

www.afm-journal.de

localized electromagnetic field can be tailored by tuning shape, size, periodicity, and composition of all-dielectric structures for broad applications such as sensing,[8] optical switching,[9] higher harmonic generation,[10,11] and color nanoprinting.[12] The advantages of all-dielectric structures over their plasmonic counterparts are attributed to their generally low intrinsic material damping and their compatibility with well-developed industrial semiconductor fabrication technologies such as complementary metal–oxide–semiconductor (CMOS).[7,13] Moreover, for monitoring of specific binding events, plasmonic materials, particularly noble metal nanoparticles, are limited by surface functionalization mainly based on functional thiol molecules. In contrast, dielectric materials offer opportunities for versatile surface functionalization using, for example, hydroxyl groups, carboxylic groups, and amine groups to realize immobilization of probe molecules. This applies particularly for silicon-based dielectric materials, which can be treated by various silane chemistries.

In pioneering reports, for example, an all-dielectric silicon metasurface made from nanodisks has been engineered for multiplexed biomarker detection at visible wavelengths on a closed optofluidic chip.[14] Another work has used silicon nanodisks to demonstrate sensing with high-affinity biotin/streptavidin bioassay, reaching a detectable concentration as low as 0.1 nM in the near-infrared spectral range.[15] However, the Q factor of such silicon nanodisk metasurfaces based on dipolar Mie resonances needs further optimization to offer a high figure of merit (FOM), specifically in the visible spectral range. The enhanced near-fields in such simple all-dielectric resonators are often confined inside the resonator volume, limiting the field overlap with the analyte, thereby reducing the light-matter interaction and the sensitivity.

Recently, the physics of bound states in the continuum (BIC) has been transferred from quantum mechanics to nanophotonics as a possible solution to overcome this challenge. BICs occur due to the destructive interference of the radiation of multiple modes involved.[16,17] An ideal BIC only exists in a mathematical sense. It is a mode characterized by an infinite Q factor that cannot be excited with radiation from the far-field. Practically, to employ this state in nanophotonics, a quasi-BIC[18] can be realized where the Q factor becomes large but finite close to the BIC condition. BIC-based nanophotonic approaches have attracted significant attention both for sensing of the local environment via either the resonance shift[19,20] or the difference of amplitude and phase of the resonance,[21] as well as the identification of molecular vibrational fingerprints in the mid-infrared spectral region.[22,23] One robust way to realize a quasi-BIC is by breaking the structural symmetry of the underlying resonators when they are ordered within an array.[24–26] In this case, either by adding a part to or removing a part from the initial symmetric shape of an individual meta-atom,[23,25] a quasi-BIC with an ultrasharp Fano lineshape can be realized.[23]

Here, we introduce a new meta-atom with an asymmetric crescent shape and then vary the curvature of one side of the crescent to approach the symmetry-protected quasi-BIC condition, showing well-controllable Q factors and electromagnetic field confinements. Besides a lowest order quasi-BIC resonance, we also exploit a higher-order mode for the purpose of sensing for the first time. The excitation of this higher-order resonance

is possible when measured in a local environment with a refractive index higher than air, such as in aqueous solutions. The refractive index of the local environment has to be large enough to shift the higher-order resonance to wavelengths longer than the wavelength below which a first diffraction order is propagating in the dielectric substrate. This spectral modification enables the observation of a high-Q higher-order resonance that is remarkably sensitive to changes in the environment. This higher-order resonance allows bulk refractive index sensitivities (BRIS) reaching 326 nm RIU^{-1}, and ultrathin biomolecular detection with a more pronounced shift than the fundamental quasi-BIC. Moreover, the sensitivity and FOM of both the fundamental quasi-BIC and the higher-order resonance can be precisely tuned via the geometry of the crescent meta-atoms. Our numerical simulations combined with these experimental results provide new insights on the design of BIC-based nanophotonic sensors and highlight the use of higher-order resonances in such systems as an additional tool for boosting their sensitivities.

2. Results and Discussion

2.1. Silicon Crescent Metasurface

All-dielectric silicon crescent metasurfaces have been fabricated on fused silica substrates by a standard top-down approach with a sequence of positive resist e-beam lithography and reactive ion etching steps (see details in Experimental Section). **Figure 1**a shows the crescent meta-atom schematically and defines the unit cell of the metasurface with a periodicity in x- (P_x) and y-direction (P_y). The footprint of the crescent meta-atom is represented by two circles, as shown in Figure 1a. A first circle (highlighted in red) with a radius of R_2 trims the area of a second circle (highlighted in blue) with a radius of R_1 (Figure 1a), resulting in the proposed crescent shape. The width (W) of this crescent shape is kept constant with a value of $R_1/3$. The exact values of W, P_x, and P_y are kept the same throughout this work. The value of the opening angle θ indicated in Figure 1a is tuned to modify the asymmetry of the crescent meta-atom. Therefore, when changing the radius of R_2, θ is changed simultaneously. The thickness of the amorphous silicon film deposited by plasma-enhanced chemical vapor deposition (PECVD) controls the height (h) of the crescent meta-atom. Figure 1b shows a high-resolution scanning electronic microscopy (HR-SEM) side-view image of the fabricated all-dielectric crescent metasurface with high structural fidelity and homogeneity (see also Figure S1, Supporting Information).

To realize quasi-BIC resonances in this metasurface, we have carried out numerical simulations using the commercial electromagnetic solver CST Microwave Studio Suite, optimizing all the relevant parameters defined in Figure 1a. We found that a crescent metasurface with $P_x = P_y = 405$ nm, $R_1 = R_2 = 180$ nm, $W = 60$ nm can realize a quasi-BIC resonance at 747 nm as indicated by the green curve (scaling factor $S = 1.0$) in Figure 1c. By a straightforward scaling of the factor S on these optimized parameters, linear tuning of the quasi-BIC resonances across a large part of the visible spectrum from 610 to 838 nm can be realized (Figure 1c). Our crescent design also provides localized near-field enhancement surrounding the surface (Figure 1b,
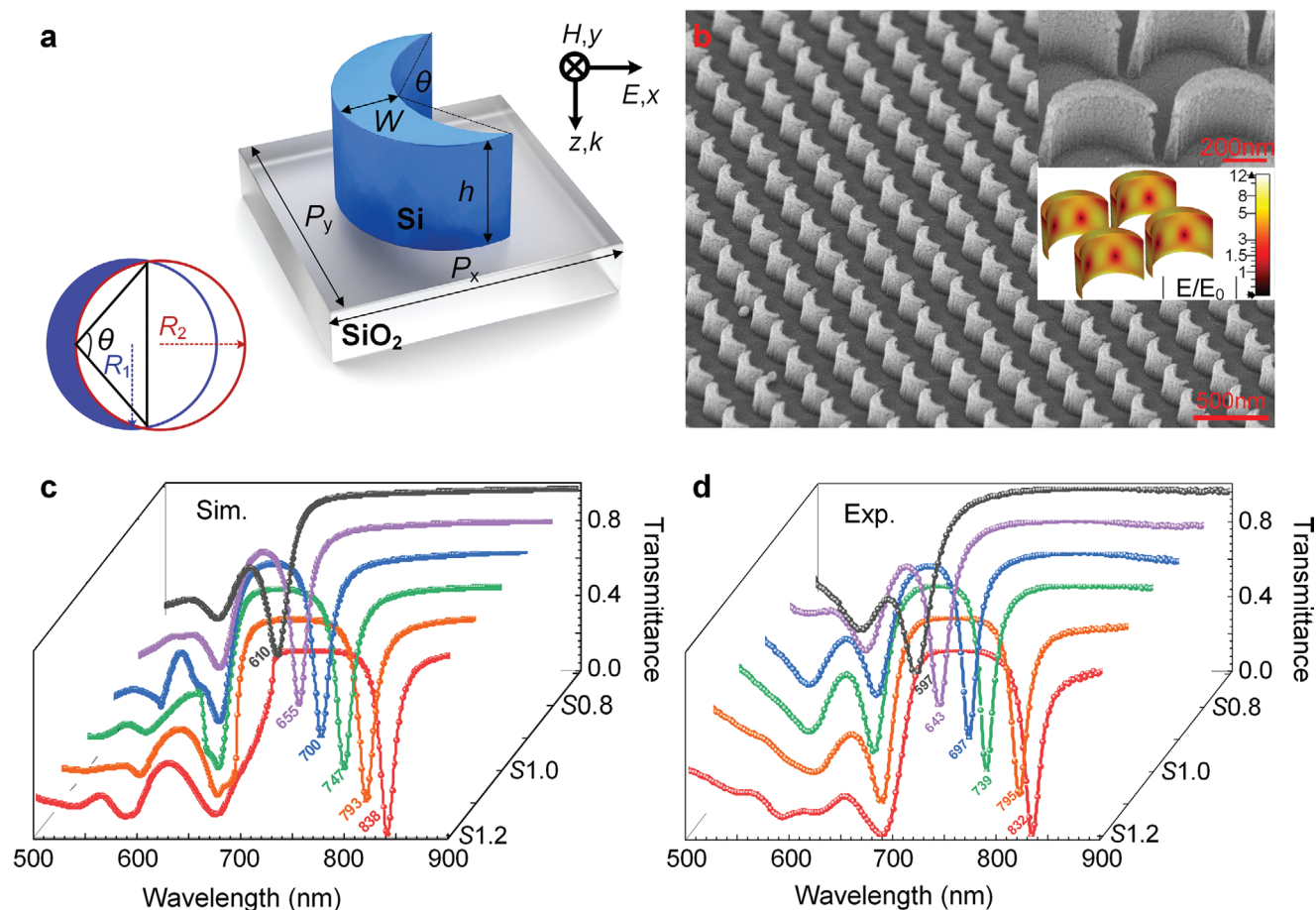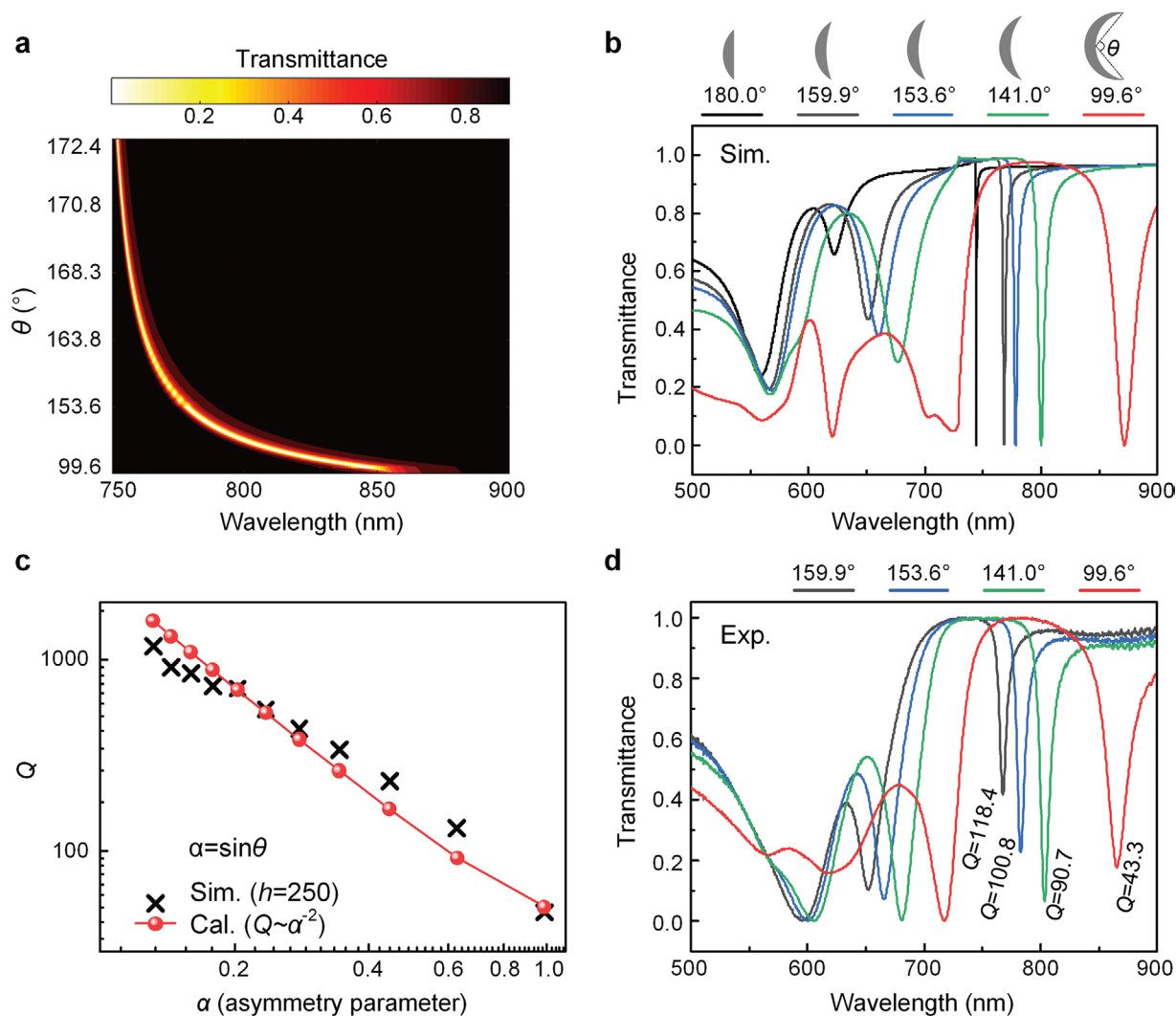
Figure 1. All-dielectric silicon crescent metasurface. a) Sketch of a unit cell with a crescent meta-atom on a fused silica (SiO_2) substrate. b) Side-view HR-SEM image of the fabricated silicon crescent metasurface with a close-up image and simulated near-field distribution of the resonator (inset). c) Simulated (Sim.) and d) experimentally (Exp.) observed transmittance spectra as a function of scaling factor (S) of the crescent meta-atom from 0.7 to 1.2 (from black curve to red curve) with a step width of 0.1.

inset). Figure 1d shows the experimentally measured transmittance spectra using the same geometrical parameters used in the simulation. A confocal microscope integrated with a spectrometer in transmission mode with collimated light illumination is used to characterize the optical properties (see Figure S2, Supporting Information). The height h of the crescent meta-atoms considered in Figure 1c,d is 250 nm. Both the experimental observations and the simulation results indicate a linear red shift of the quasi-BIC resonance with increasing the scaling parameter S from 0.7 to 1.2, which is consistent with previous work.[23] As expected, we also observe a broadening of the FWHM when the resonant wavelength is blue-shifted below 650 nm in both simulations and experiments, which we attribute to the silicon interband loss in that wavelength region (< 660 nm). Figure S3, Supporting Information compares the Q factor (defined as $Q = \lambda_0/\text{FWHM}$, where is λ_0 the resonance position) as a function of S between the simulation and experiment. With increasing S, the Q factor improves as expected, due to the reduced intrinsic absorption loss of silicon. The Q factor of the quasi-BIC can be tuned precisely by breaking the in-plane symmetry of the underlying crescent resonators,[26] which is investigated in the following section.

2.2. Symmetry-Protected Quasi-BIC of the Crescent Metasurface

The crucial parameter characterizing the meta-atom is the opening angle θ. It is the vertex angle of an isosceles triangle raised by the two intersection points of two circles connected with the third point at the midpoint of the one side of the crescent (indicated in Figure 1a, inset). θ defines the asymmetry of this crescent shape, where θ is tuned by varying R_2. With increasing R_2, θ is also increased, making the crescent meta-atom nearly symmetric but not reaching a completely symmetric case. **Figure 2**a shows the simulated wavelength dependent transmittance of the crescent metasurface with varying θ. The FWHM at the resonant wavelengths becomes much narrower with slight blue shifts with an increase in θ. The blue shift of the quasi-BIC resonances can be explained by the decreased volume of the meta-atom with increasing θ. Note that the values of θ indicated in the transmittance map (Figure 2a) are calculated from the value of R_2, which is set to $1.0R_1$, $2.0R_1$, $3.0R_1$, $4.0R_1$, $5.0R_1$, and $6.0R_1$. Several representative crescent shapes with different θ, where R_2 equals $1.0R_1$, $1.5R_1$, $2.0R_1$, $2.5R_1$, and an infinite value with the limiting case of $\theta = 180°$ from right to left and their corresponding simulated

ADVANCED
SCIENCE NEWS
www.advancedsciencenews.com

ADVANCED
FUNCTIONAL
MATERIALS
www.afm-journal.de

Figure 2. Symmetry-protected quasi-BIC resonances of the crescent metasurface. a) Wavelength-dependent transmittance of the metasurface with $S = 1.2$, $h = 300$ nm, and varying θ. b) Individual transmittance spectra were taken from the resonance map in panel (a) for selected samples. Schematics in the top row shows different crescent shapes with varying θ for illustrative purpose. We can observe a reduced FWHM at the resonant wavelength with increasing θ. c) Q as a function of the asymmetry parameter (α) and a demonstration of an agreement of Q between the simulation (black curve) and calculation (red curve), where the $\alpha = \sin\theta$. d) Experimental transmittance spectra with narrowed FWHM of different crescent shapes ($S = 1.2$, $h = 300$ nm) with increasing θ. The value of Q is indicated for each quasi-BIC resonance.

transmittance spectra are shown in Figure 2b. The smallest FWHM has been observed at the limiting case of $\theta = 180°$, even though the point of perfect symmetry[17] (i.e., a symmetric convex lens-shaped particle) has not been reached. For the symmetric case, the Q factor would approach infinity, reaching the BIC case and thus resulting in a resonance that can no longer be excited from the far-field.

To further analyze the scaling behavior of the Q factor, we can define an asymmetry parameter $\alpha = \sin\theta$ (Figure 2c). We found that the estimated Q factor from the simulation follows the characteristic quasi-BIC behavior of $Q \propto (\sin\theta)^{-2}$ very well.[26] However, there is a slight variation of the Q factor between the simulation results (black curve, Figure 2c) and the calculated ones (red curve, Figure 2c). This variation is attributed to the simplicity in defining the asymmetric parameter α that we evaluate numerically with full-wave solutions to the Maxwell

equations. It is worth noting that the first calculated point in Figure 2c, $R_2 = 6.0R_1$ is taken, which results in an asymmetry parameter of $\theta = 172.4°$. This explains why we do not observe divergent behavior of the BIC resonance from the empirical equation. Also, the limiting case of a crescent shape with $\theta = 180°$ does not result in an ideal BIC with a negligible FWHM and an infinite Q factor. This perfect BIC can only be reached for a symmetric lens-shaped meta-atom. The good agreement of the Q factor for varying θ between simulation and analytical calculation indicates that the behavior of our all-dielectric crescent metasurface can be explained within the framework of symmetry-protected BICs. Furthermore, we have demonstrated experimentally the excitation of quasi-BICs via crescent shaped meta-atoms (Figure 2d). Indeed, with increasing θ, the FWHM is continuously narrowed with a corresponding improved Q factor (values indicated directly in Figure 2d). The experimental

ADVANCED
SCIENCE NEWS
www.advancedsciencenews.com

ADVANCED
FUNCTIONAL
MATERIALS
www.afm-journal.de

Q factor reaches the highest value of ≈120 at visible wavelengths with $\theta = 159.9°$ ($2.5R_1 = R_2$) compared to 256 in simulation. We attribute this decrease of the experimental Q factor to fabrication variations of the unit cell geometrical parameters and associated imperfections in the fabricated samples. In the following, unless indicated otherwise, a value of $\theta = 99.6°$ ($R_1 = R_2$) is fixed for all metasurface designs.

2.3. Bulk Refractive Index Sensing

To evaluate the sensing performance of the fabricated all-dielectric crescent metasurface, we have first quantified the bulk refractive index sensing capabilities of the metasurface. Specifically, we have immersed the metasurface in a glycerol-water mixture with varying refractive index. Besides the expected quasi-BIC resonance at long wavelengths, we found that a higher-order resonance at shorter wavelengths can be excited. This resonance shows an even more significant shift in response to environmental refractive index changes Δn in comparison to the resonance at longer wavelengths, as highlighted in **Figure 3**a. To simplify the following discussion, we denote the resonance at longer wavelength as the first-order resonance (first-order or fundamental order), and the resonance at shorter wavelengths as the second-order resonance (second-order or higher-order), respectively. The reasoning for this terminology can be justified by inspecting the electric and magnetic field distributions surrounding the crescent meta-atoms at the respective resonance wavelengths with a refractive index of $n_{env.} = 1.333$ for the surrounding environment (Figure 3b, and Figure S4, Supporting Information). When looking at the field components not contained in the incident field in the x-y plane at $z = 20$ nm above the metasurface, we see a systematic increase in the complexity of the field pattern from the fundamental resonance wavelength to the higher-order one. Specifically, the y-component of the electric field amplitude of the first-order resonance has a single node, whereas the second-order mode exhibits three nodes. We note that only an even number of nodes are permissible for the symmetric particle. Similar to the behavior of the nodes in the y-component, the z-component of the electric field shows an increasing number of amplitude peaks with increasing resonance order. This is consistent with the behavior of ordinary nanodisk resonators, where higher-order modes with an increasing number of field nodes are supported at higher frequencies. The behavior had also been observed for other structures such as split-ring resonators.[27] In fact, the crescent structure can support resonances higher than the second-order if the surrounding refractive index is increased even further (Figures S5 and S6, Supporting Information). However, when working in an aqueous solution ($n_{env.} = 1.333$), these even higher-order resonances occur at wavelengths below the characteristic wavelength of the first diffraction order associated with the array periodicity, preventing them from manifesting in the spectrum of observation for which the metasurface has a subwavelength period.

The numerical simulations (Figure 3b) concerning the transmission at different refractive indices of the surrounding medium show an excellent agreement with the experimental observation (Figure 3a). The fundamental quasi-BIC and the higher-order resonance are excited when the crescent metasurface is exposed to a bulk medium. Still, the higher-order resonance shift is about two times larger than the fundamental quasi-BIC (close-up images, Figure 3c). This is the first report that leverages multiple co-existing resonances for a sensing application to the best of our knowledge.

To further evaluate the suitability of the fundamental quasi-BIC and the higher-order resonance for sensing, the impact of the parameters of S and h of the crescent meta-atom have been investigated (Figure 3d). Figure S7, Supporting Information shows the measured transmittance spectra of corresponding crescent meta-atom with different S ($S = 0.9$, 1.1, 1.2, and 1.3) in response to a bulk medium with changing n. To evaluate the BRIS performance, the sensitivity ($s = \Delta\lambda/\Delta n$ in units of nm RIU^{-1}) has been calculated, where $\Delta\lambda$ is a change of resonant wavelength in response to a change of bulk refractive index Δn. As stated above, the higher-order resonances can be observed only when they occur at wavelengths for which the metasurface is subwavelength in both transmission and reflection. This requirement explains why the higher-order resonances were not observed for metasurfaces made from crescent meta-atoms with a smaller scaling factor. Meta-atoms with small scaling factors shift the resonances to shorter wavelengths, which prevents their excitation. Besides, the higher-order resonance always shows a higher sensitivity, which is about two times larger than that of the fundamental quasi-BIC resonance. The highest sensitivity caused by such a higher-order resonance can reach 326 nm RIU^{-1}, higher than the previously reported quasi-BIC driven sensing in the visible region with 263 nm RIU^{-1}.[20] It highlights the importance of considering such higher-order resonances as an additional toolkit for the design of high-performance nanophotonic sensors.

Additionally, to demonstrate why the higher-order resonance shows a higher sensitivity for the bulk refractive index sensing, crescent shapes with three different θ (when $R_2 = 1.0R_1$, $R_2 = 1.5R_1$ and $R_2 = 2.0R_1$) have been experimentally realized. Results are presented in **Figure 4**a and Figure S8, Supporting Information. Moreover, numerical simulations have been performed for identical geometries (Figures S5, S6, and S8, Supporting Information). Intriguingly, it was observed that the higher-order resonance does not always show a larger shift than the fundamental quasi-BIC resonances for every different geometry of the crescent meta-atoms. To shed more light on this surprising behavior, the electric near-field intensity confined to the resonators has been monitored in numerical simulations since the electric field intensity outside the resonator is responsible for its sensitivity, according to perturbation theory[28]

$$\frac{\delta\omega}{\omega_0} \approx \frac{\int_{V_{out}}[\varepsilon_{out}(\mathbf{r}) - \varepsilon_0(\mathbf{r})]\left|\mathbf{E}(\mathbf{r},\omega_0)\right|^2 dV}{\int_{V_{all}}\varepsilon_0(\mathbf{r})\left|\mathbf{E}(\mathbf{r},\omega_0)\right|^2 dV} \tag{1}$$

where ω_0 is the initial resonance frequency, $\delta\omega$ is the resonance shift, ε_{out} and ε_0 are the permittivity distribution of the metasurface in the presence of the modified local environment and the permittivity of the initial surrounding medium, respectively. $\mathbf{E}(\mathbf{r}, \omega_0)$ is the electric field of the mode sustained in the resonator. V_{all} represents a cube with a volume of $P_x \times P_y \times 450$ nm^3, where the height of 450 nm includes the resonator height
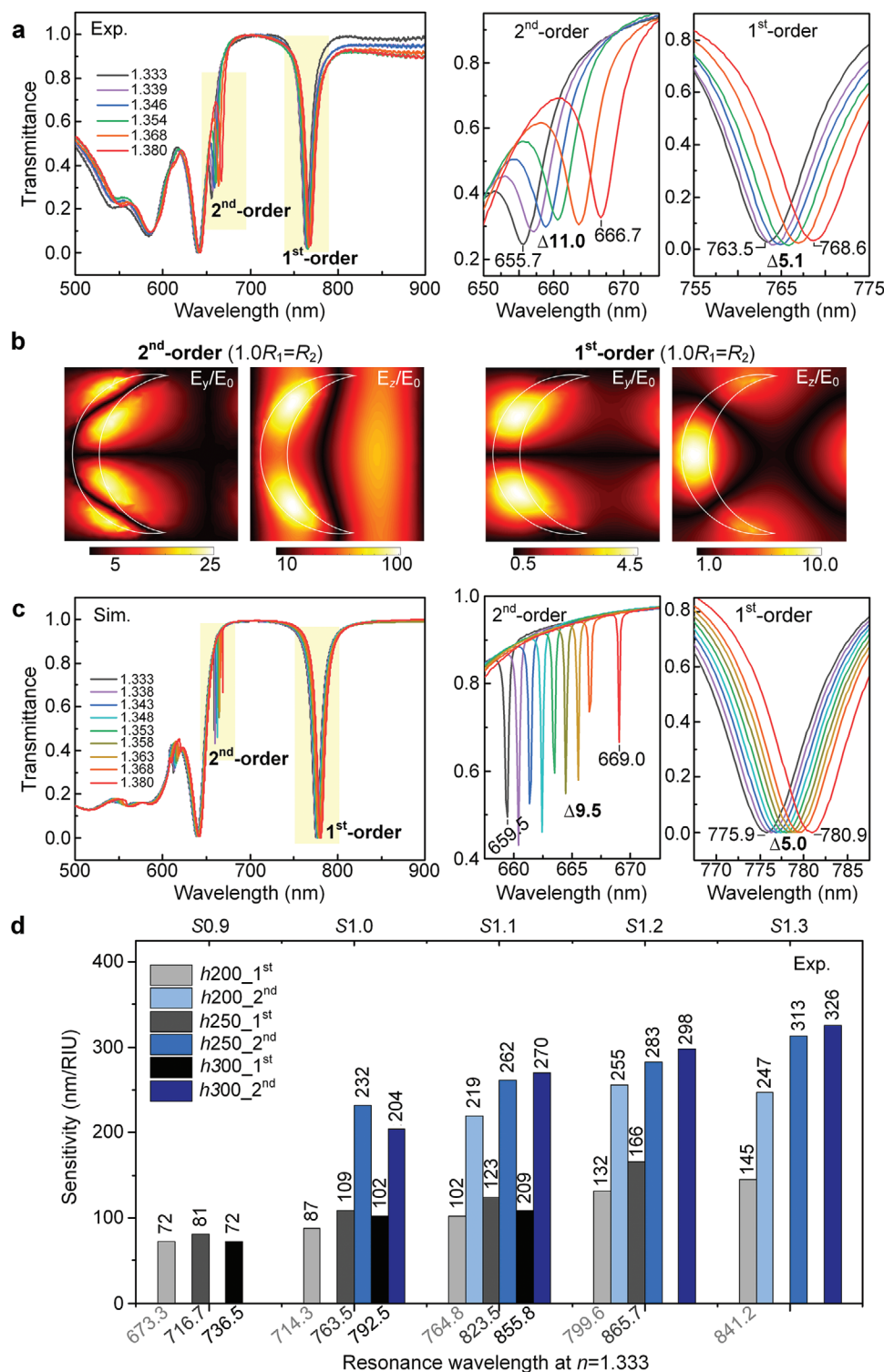
Figure 3. Bulk refractive index sensing using the fabricated crescent metasurface ($\theta = 99.6°$, when $R_1 = R_2$). a) Experimental transmittance spectra in response to a bulk medium with different $n_{env.}$ and their corresponding close-up images highlighting the first-order and second-order resonance shifts. b) Distribution of the electric field components E_y and E_z evaluated 20 nm above the crescent metasurface in water ($n_{env.} = 1.333$). c) Simulated transmittance spectra corresponding to (a), using the same crescent structural geometries ($S = 1.0$, $h = 250$ nm). Close-up images in (a) and (c) show the relative resonance shifts of the first-order and second-order resonance. d) Sensitivity (s) of the crescent metasurface for the fundamental quasi-BIC and the higher-order resonances. The x–axis indicates their fundamental quasi-BIC resonant position when the metasurface is exposed to a bulk medium with $n_{env.} = 1.333$. The top x–axis indicates the dimensions of the crescent structure by tuning S. The heights h of the crescent resonators are indicated by a gradient color of light grey/blue (200 nm), medium grey/blue (250 nm), and dark grey/blue (300 nm). The grey (blue) color bars indicate the first-order (second-order) sensitivity.
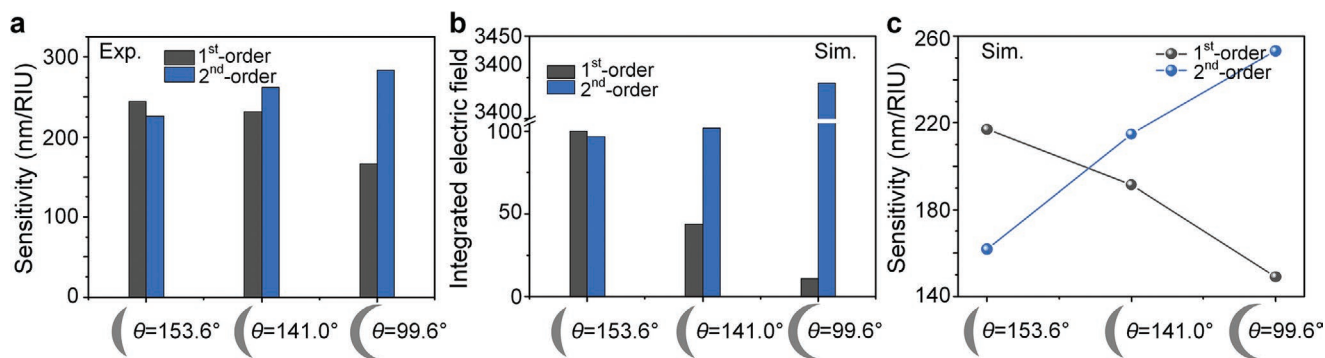
Figure 4. Controllable BRIS of the crescent metasurface ($S = 1.2$ and $h = 250$ nm). a) BRIS of a crescent shape with different θ (indicated below). The black (blue) bars show the first-order (second-order) resonance sensitivity. b) Simulated integrated electric field intensity over outside the resonator, and c) the corresponding sensitivity of metasurfaces for different crescent shapes. The used dimension parameters for the simulation are the same as in experiment (a).

(250 nm) and a volume above the resonator top surface with a height of 200 nm. The outside volume V_{out} is given by the total volume (V_{all}) minus the resonator volume.

Hence, from the values of $\frac{\mathbf{E}_{out}^2}{\mathbf{E}_{all}^2} \times \frac{\mathbf{E}_{all}^2}{\mathbf{E}_{all,0}^2}$ for the crescent meta-atoms with varying θ at their resonant wavelengths when $n_{env.} = 1.333$ (Figure 4b), we conclude that, indeed, the stronger the electric field confinement outside the resonator, the higher the sensitivity. Here, $\mathbf{E}_{out}^2$ is the integrated intensity of the electric field across the spatial domain outside the resonator, and $\mathbf{E}_{all}^2$ represents the integrated electric field intensity in free space with a particular volume of $P_x \times P_y \times 450$ nm^3 containing the resonator and the surrounding space. $\mathbf{E}_{all,0}^2$ was obtained by setting the same metasurface in a homogenous environment with $n_{env.} = 1.333$ in numerical simulation. The sensitivity of the crescent metasurface with different θ in simulation is in good agreement with the experimental values, further indicating that the electric field enhancement strongly determines the sensitivity of an optical sensor.

It is worth noting that the first- and second-order resonances exhibit an inverse behavior in terms of the electric field intensity outside of the resonator as a function of the geometrical parameters (Figure 4b). This can be explained by the different effects of a decrease in R_2 and correspondingly θ on the in-plane symmetry of the crescent meta-atom. For the fundamental resonance, a decrease of R_2 implies a further departure from the symmetric lens-shaped structure, as discussed above, with the subsequent decrease in the quasi-BIC Q factor and the near-field intensity. On the other hand, the inverse behavior of the higher-order resonance compared to the fundamental quasi-BIC resonance is attributed to the interference of different resonant phenomena related to the change of crescent curvature via changing R_2, and the resulting interactions on such a periodic array. It points to the fact that the actual optical properties of the particle when placed in the lattice, which strongly modifies the optical properties of the particle even further, can strongly affect the overall response. But independent of these details, the design procedure, as well as the selection of the surrounding medium enable the excitation of two resonances, a fundamental and a higher-order one, with opposite response to a change in θ. The simultaneous appearance unlocks additional degrees of

freedom in designing optical metasurface with well-tailored Q factor and strongly enhanced near-fields ideal for sensing.

2.4. Biomolecular Sensing

Our dielectric crescent meta-atoms efficiently concentrate electromagnetic fields on the nanoscale, comparable in size to many relevant biomolecules. Thus, they show high potential for the detection of ultrathin biomolecular layers. Also, since the dimensions of the crescent meta-atoms can fully control the characteristic metasurface resonance frequency, such approaches are ideally suited for multiplexed label-free bioassays, where multiple analytes are sensed simultaneously. Besides, it holds tremendous potential for integration into microfluidic chips for developing clinical point-of-care devices.

A high affinity biotin-streptavidin bioassay has been chosen to demonstrate the detection of an ultrathin biomolecular layer (see Experimental Section). There is an obvious red shifting with each step of surface functionalization when the detection takes place in air (**Figure 5**a). The final resonance shifts (relative shift of the streptavidin immobilized metasurface to the previous step of biotin-treated metasurface) in response to target analyte with different concentrations are shown in Figure 5b. They indicate that target analyte concentration as low as 0.167 nM can be distinguished. This minimal measurable concentration is comparable to previous reports working at near-infrared wavelengths.[15] The obtained calibration curve was fitted using a four-parameter logistic equation with a correlation coefficient of 0.999. The estimated sensitivity can be obtained from this fitting curve, which is the slope of the dose-response in the dynamic quantification range with 1.5 nm nM^{-1} for streptavidin.

The monitoring of biomolecular binding in real-time often occurs in a buffer environment, which reduces the refractive index contrast and leads to decreased sensitivity according to Equation (1). To reveal the capability of the higher-order resonance for biomolecular sensing in a buffer environment ($n \approx 1.333$), the total resonance shifts in buffer were monitored as shown in Figure 5c. The shift of the resonance dip is more evident for the higher-order one than the fundamental one due to the narrower FWHM. Even though the resonance shifts observed in the
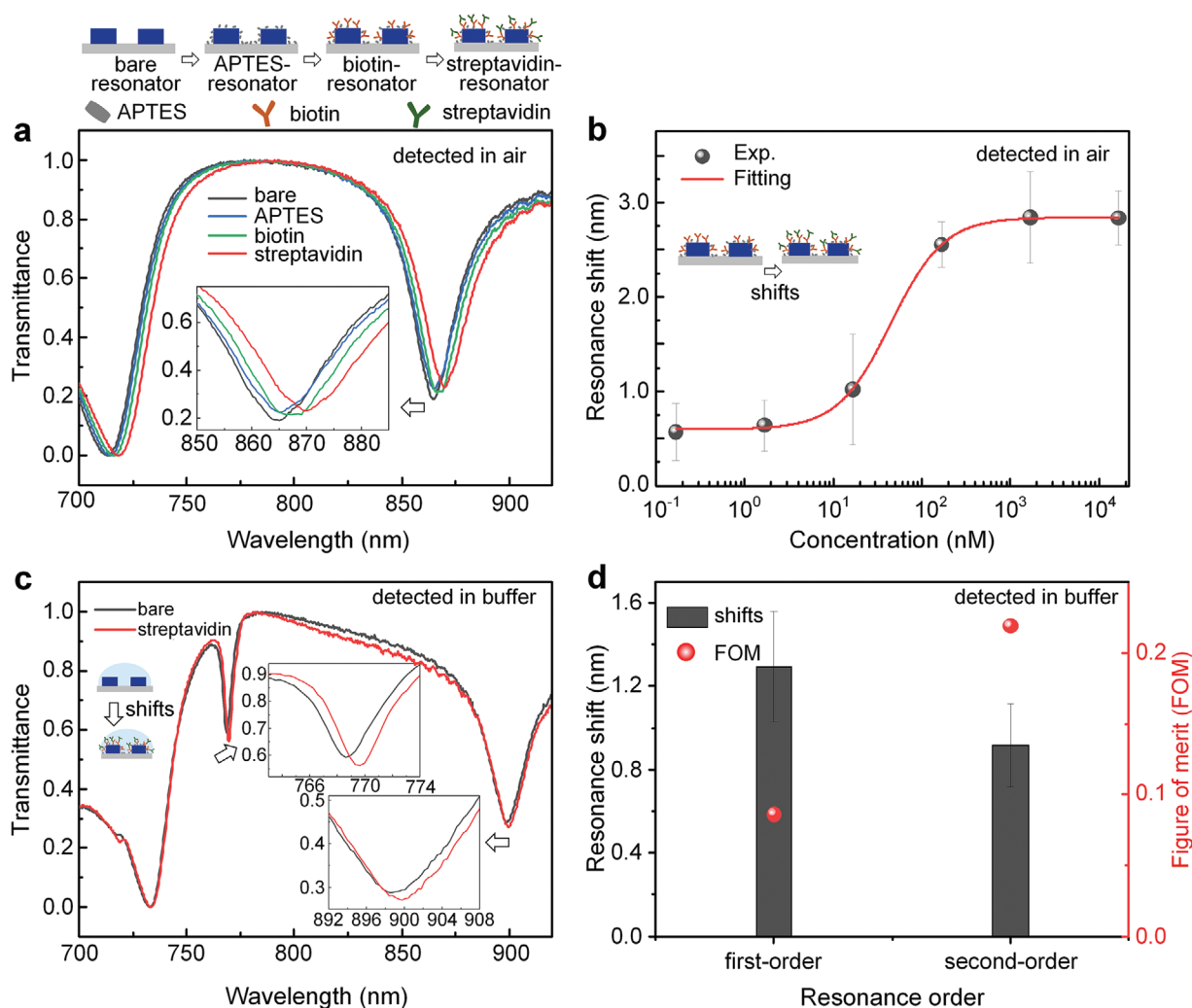
Figure 5. All-dielectric crescent metasurface for ultrathin biomolecular layer sensing. a) Transmittance spectra of the sensor over the sequence of molecule immobilization steps. b) Final relative resonance shifts in response to different streptavidin concentrations for detection in air. c) Transmittance spectra of the bare sensor and the biotin-streptavidin immobilized sensor when detected in the buffer. d) Comparison of resonance shifts and corresponding FOM of the first-order and second-order resonances in the buffer. A streptavidin concentration of 1.67 μM was used in (a), (c), and (d). Three replicates from different crescent metasurface fields were tested for each data point. Error bars represent the standard deviation.

buffer are less than in air, this can be further improved by implementing a sandwich biomolecular assay.[29] Figure 5d compares both resonance shifts and their corresponding FOM (defined as FOM = resonance shift/FWHM), indicating a clear advantage of employing this higher-order resonance in biosensing, owing to its higher value of FOM compared to the first-order resonance.

3. Conclusion

We have developed an all-dielectric silicon crescent metasurface driven by quasi-BICs and demonstrated it as an efficient optical sensing platform. By tuning the asymmetry of the crescent meta-atoms, the symmetry-protected BIC was transformed into an accessible quasi-BIC with a tunable Q factor and enhanced near-fields. Consequently, the enhanced light-matter interaction was shown to produce a high BRIS of 326 nm RIU^{-1} as well as the capability for the detection of ultrathin layers of biomolecules down to sub-nanomolar concentrations. More

importantly, besides leveraging the fundamental quasi-BIC resonance, a higher-order resonance has also been excited simultaneously and employed for monitoring a sensing event in a buffer environment, which provides excellent FOM due to the ultrasharp resonance. The fundamental quasi-BIC and the higher-order resonances supported by such crescent metasurfaces can be well-tuned concerning their Q factor and the near-field enhancement by tailoring the geometry of the crescent meta-atom, making them ideal for a wide range of practical applications. Our findings open a novel avenue for developing quasi-BIC driven all-dielectric metasurfaces as optical sensors for real-time and in situ detection in an optofluidic chip, with the potential for applications in clinical diagnostics.

4. Experimental Section

Numerical Simulations: The optical behavior of the all-dielectric silicon metasurface consisting of crescent meta-atoms was simulated

**ADVANCED
SCIENCE NEWS**

www.advancedsciencenews.com

**ADVANCED
FUNCTIONAL
MATERIALS**

www.afm-journal.de

by frequency-domain finite-element method Maxwell solver from CST STUDIO SUITE 2020. To improve the agreement between simulation and experiment, measured values of the silicon permittivity from ellipsometry were considered in the simulation. For the illumination, a plane wave at normal incidence to the metasurface with linear polarization in the x-direction (along the axis of crescent meta-atom width, indicated in Figure 1a) was considered. A 2D periodicity defined the unit cell in the x– and y– axis with $P_x = P_y = 405$ nm. The crescent width was $W = R_1/3$ ($R_1 = 180$ nm). The refractive index of fused silica serving as supporting substrate was taken as 1.5.

All-Dielectric Silicon Metasurface Fabrication: A layer of amorphous silicon (a-Si) film was deposited on the commercial fused silica substrate by PECVD, where the film thickness can be precisely controlled, and this determined the resulting resonator height (h). The patterning of crescent resonators was carried out by electron beam lithography in spin-coated single-layer positive photoresist of PMMA (PMMA 950 K) film using 30 kV acceleration voltage and 10 μm aperture. A protection layer of SiO_2 (10 nm) and chrome (Cr) (50 nm) as a hard mask was deposited via electron beam evaporation before reactive ion etching. Subsequently, a wet chemical lift-off process was followed using solvent 1165 (The Dow Chemical Company) at 80 °C for 2 h. Then the resulting pattern was transferred to a Plasmalab 100 system from Oxford Instruments for silicon etching, where Ar (7 sccm) and Cl_2 (20 sccm) as etching gases were applied under 20 W bias power and 200 W induction power at 20 °C. The remaining Cr hard mask was removed by chemical wet etching, and the remaining SiO_2 hard mask was etched by reactive ion etching, applying Ar (30 sccm) and CHF_3 (20 sccm) as etching gases under 30 W bias power at 20 °C, which resulted in an all-dielectric silicon metasurface.

Biomolecule Binding: Specific molecular detection using the fabricated all-dielectric silicon metasurface has been realized, which involves three steps: surface activation, probe immobilization, and target capture. High affinity biotin-streptavidin biomolecules were applied in this work. First, the metasurface was treated by piranha solution (a mixture of H_2O_2 and H_2SO_4 with a volume ratio of 1:3) for more than 2 h and followed by O_2 plasma (Fetoma) with 100% power for 10 min to generate hydroxyl radicals (-OH) on the metasurface. Afterwards, the metasurface was immersed into ethanol containing 10 v/v (3-aminopropyl)triethoxysilane (APTES) for 2 h, and after that, was rinsed by ethanol for 1 min, dried by a stream of nitrogen gas, and heated at 110 °C for 1 h. The probe molecule of sulfo-NHS-biotin (ThermoFisher Scientific, Mn = 443.4) dissolved in phosphate buffered saline (1 × PBS) buffer (Sigma Aldrich) was drop-casted on the metasurface with a volume of 40 μL for 2 h at room temperature. Then, biotin-immobilized metasurface was rinsed by 1 × PBS buffer and dried by a stream of N_2 flow, and subsequently incubated in streptavidin (Sigma Aldrich) with a varying concentration in a range of (≈0.167 nM–16.7 μM) for 2 h at room temperature. After the streptavidin incubation, the metasurface was also rinsed by 1 × PBS buffer, dried by a stream of N_2 flow, and transferred for optical characterization. After each step of functionalization, the transmittance spectra were recorded from three different samples.

Optical Characterization: The optical performance of all-dielectric metasurfaces was characterized by a spectrometer equipped on a confocal microscope (WITec, Germany). A collimated white light source illuminated the metasurface, and the spectra were collected in transmission mode with a linear polarizer. The transmittance spectra were obtained by normalizing the signals of the arrays to that of the unpatterned area.

Supporting Information

Supporting Information is available from the Wiley Online Library or from the author.

Acknowledgements

Conflict of Interest

The authors declare no conflict of interest.

Data Availability Statement

Data available on request from the authors.

Keywords

[1] D. Rodrigo, A. Tittl, N. Ait-Bouziad, A. John-Herpin, O. Limaj, C. Kelly, D. Yoo, N. J. Wittenberg, S. H. Oh, H. A. Lashuel, H. Altug, *Nat. Commun.* **2018**, *9*, 2160.

[2] J. N. Anker, W. P. Hall, O. Lyandres, N. C. Shah, J. Zhao, R. P. Van Duyne, *Nat. Mater.* **2008**, *7*, 442.

[3] K. I. Macconaghy, C. I. Geary, J. L. Kaar, M. P. Stoykovich, *J. Am. Chem. Soc.* **2014**, *136*, 6896.

[4] A. J. Haes, S. Zou, G. C. Schatz, R. P. Van Duyne, *J. Phys. Chem. B* **2004**, *108*, 6961.

[5] A. I. Kuznetsov, A. E. Miroshnichenko, M. L. Brongersma, Y. S. Kivshar, B. Luk'yanchuk, *Science* **2016**, *354*, aag2472.

[6] A. E. Miroshnichenko, A. B. Evlyukhin, Y. F. Yu, R. M. Bakker, A. Chipouline, A. I. Kuznetsov, B. Luk'yanchuk, B. N. Chichkov, Y. S. Kivshar, *Nat. Commun.* **2015**, *6*, 8069.

[7] M. Decker, I. Staude, *J. Opt.* **2016**, *18*, 103001.

[8] A. Tittl, A. John-Herpin, A. Leitis, E. R. Arvelo, H. Altug, *Angew. Chem., Int. Ed.* **2019**, *58*, 14810.

[9] S. Han, L. Cong, Y. K. Srivastava, B. Qiang, M. V. Rybin, A. Kumar, R. Jain, W. X. Lim, V. G. Achanta, S. S. Prabhu, Q. J. Wang, Y. S. Kivshar, R. Singh, *Adv. Mater.* **2019**, *31*, e1901921.

[10] T. Ning, X. Li, Y. Zhao, L. Yin, Y. Huo, L. Zhao, Q. Yue, *Opt. Express* **2020**, *28*, 34024.

[11] G. Grinblat, Y. Li, M. P. Nielsen, R. F. Oulton, S. A. Maier, *Nano Lett.* **2016**, *16*, 4635.

[12] Y. Nagasaki, M. Suzuki, J. Takahara, *Nano Lett.* **2017**, *17*, 7500.

[13] D. Ray, T. V. Raziman, C. Santschi, D. Etezadi, H. Altug, O. J. F. Martin, *Nano Lett.* **2020**, *20*, 8752.

[14] O. Yavas, M. Svedendahl, P. Dobosz, V. Sanz, R. Quidant, *Nano Lett.* **2017**, *17*, 4421.

[15] N. Bontempi, K. E. Chong, H. W. Orton, I. Staude, D. Y. Choi, I. Alessandri, Y. S. Kivshar, D. N. Neshev, *Nanoscale* **2017**, *9*, 4972.

[16] D. C. Marinica, A. G. Borisov, S. V. Shabanov, *Phys. Rev. Lett.* **2008**, *100*, 183902.

[17] C. W. Hsu, B. Zhen, A. D. Stone, J. D. Joannopoulos, M. Soljacic, *Nat. Rev. Mater.* **2016**, *1*, 16048.

[18] M. Rybin, Y. Kivshar, *Nature* **2017**, *541*, 164.

[19] Y. Zhong, L. Du, Q. Liu, L. Zhu, K. Meng, Y. Zou, B. Zhang, *RSC Adv.* **2020**, *10*, 33018.

[20] F. Yesilkoy, E. R. Arvelo, Y. Jahani, M. Liu, A. Tittl, V. Cevher, Y. Kivshar, H. Altug, *Nat. Photonics* **2019**, *13*, 390.

[21] Y. K. Srivastava, R. T. Ako, M. Gupta, M. Bhaskaran, S. Sriram, R. Singh, *Appl. Phys. Lett.* **2019**, *115*, 151105.

[22] A. Leitis, A. Tittl, M. Liu, B. H. Lee, M. B. Gu, Y. S. Kivshar, H. Altug, *Sci. Adv.* **2019**, *5*, eaaw2871.

[23] A. Tittl, A. Leitis, M. Liu, F. Yesilkoy, D. Y. Choi, D. N. Neshev, Y. S. Kivshar, H. Altug, *Science* **2018**, *360*, 1105.

[24] K. Koshelev, Y. Tang, K. Li, D. Y. Choi, G. Li, Y. Kivshar, *ACS Photonics* **2019**, *6*, 1639.

[25] S. Li, C. Zhou, T. Liu, S. Xiao, *Phys. Rev. A* **2019**, *100*, 63803.

[26] K. Koshelev, S. Lepeshov, M. Liu, A. Bogdanov, Y. Kivshar, *Phys. Rev. Lett.* **2018**, *121*, 193903.

[27] C. Rockstuhl, F. Lederer, C. Etrich, T. Zentgraf, J. Kuhl, H. Giessen, *Opt. Express* **2006**, *14*, 8827.

[28] I. Teraoka, S. Arnold, *J. Opt. Soc. Am. B* **2006**, *23*, 1381.

[29] F. Zang, Z. Su, L. Zhou, K. Konduru, G. Kaplan, S. Y. Chou, *Adv. Mater.* **2019**, *31*, 1902331.